J Adv Ceram

Research Article

Sc^{3+}-modified Mg–Al–Mn–Fe–O spinel ceramics with co-enhanced microwave dielectric and thermosensitive properties for multifunctional applications

Wenyuan Li[1,2,†], Yue Xian[1,2,†], Hanao Deng[1], Jianan Xu[1,2], Yaxin Wei[1], Aimin Chang[1], Bo Zhang[1,✉]

Cite this article: Li W, Xian Y, Deng H, et al. *J Adv Ceram* 2025, **14**(10): 9221153. https://doi.org/10.26599/JAC.2025.9221153

ABSTRACT: With the rapid development of communication technology, multifunctional ceramics that integrate microwave dielectric and negative temperature coefficient (NTC) thermistor properties have met the evolving needs of electronic components. Although conventional spinel oxides excel in single functionalities, they struggle to simultaneously achieve linear NTC behavior and stable microwave dielectric performance over a wide temperature range. To address this, the role of Sc^{3+} substitution in modifying $Mg_{0.8}Mn_{0.2}Al_{1.6}Fe_{0.4}O_4$ ceramics was systematically investigated. The results demonstrate that Sc^{3+} substitution effectively inhibits oxygen vacancy formation and achieves the ratio regulation of the Mn^{2+}/Mn^{3+} and Fe^{3+}/Fe^{2+} bimetallic redox pairs, which significantly improves the material constant B ($B_{200/1000°C}$ = 8367–9758 K) and enables linear resistance–temperature curves (lnρ–1000/T) within a broad temperature range (200–1000 °C). Additionally, the ceramics exhibit optimal microwave dielectric properties: low dielectric constants (ε_r = 8.86–10.55), ultrahigh quality factors ($Q{\cdot}f$ = 96,000–149,000 GHz), and near-zero temperature coefficients of resonant frequency (τ_f = −33.2×10^{-6} to −10.2×10^{-6} °C^{-1}), resulting from Sc^{3+}-induced lattice stabilization and octahedral bond-valence strengthening effects. A cylindrical dielectric resonator antenna (CDRA) fabricated from $Mg_{0.8}Mn_{0.2}Al_{1.3}Sc_{0.3}Fe_{0.4}O_4$ achieves 92% radiation efficiency and 6.28 dBi gain at 12 GHz, validating its potential for Ku-band satellite communication. This work reveals that Sc^{3+} substitution synergistically enhances both the microwave dielectric and thermosensitive functionalities of Mg–Al–Mn–Fe–O spinel ceramics, offering a breakthrough in material design for next-generation multifunctional communication devices.

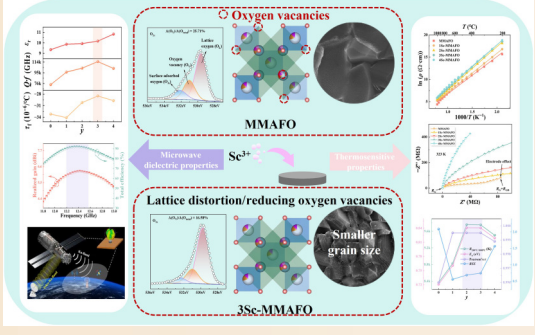

KEYWORDS: microwave dielectric properties; negative temperature coefficient; spinel; multifunctional ceramics

1 Introduction

The rapid advancement of communication technology has become a cornerstone for promoting the development of the digital economy [1–3]. As the technological paradigm has evolved from the internet of everything (IoE) to the space–air–ground–sea-integrated network (SAGSIN), multifunctional ceramics have emerged as pivotal dielectric materials to overcome critical bottlenecks in next-generation communication systems through synergistic integration of material properties and technological innovations. Although significant progress has been made in the development of multifunctional ceramics, including magnetic–microwave dielectric [4,5], ferroelectric–luminescent [6,7], magnetic–thermosensitive [8], and piezoelectric–transparent [9,10] ceramics, the integration of microwave dielectric and negative temperature coefficient (NTC) thermosensitive functionalities remains an uncharted territory. Microwave dielectric ceramics have garnered substantial research interest in microwave communication applications (shown in Fig. S1 in the Electronic Supplementary Material (ESM)), primarily owing to three key characteristics: 1) tunable dielectric constants (ε_r) that satisfy device miniaturization requirements, 2) high $Q{\cdot}f$ values (where Q = 1/tanδ, and f represents the resonant frequency) enabling enhanced frequency selectivity, and 3) near-zero temperature coefficients of resonant frequency (τ_f) ensuring thermal stability [11,12]. Simultaneously, NTC thermistors have established themselves as indispensable "thermal managers" in communication systems, offering high precision, rapid response, broad operational temperature ranges, and cost effectiveness. Given these properties, the development of

† Wenyuan Li and Yue Xian contributed equally to this work.

[1] Key Laboratory of Functional Materials and Devices for Special Environmental Conditions (Chinese Academy of Sciences), Xinjiang Key Laboratory of Electronic Information Materials and Devices, Xinjiang Technical Institute of Physics & Chemistry, Chinese Academy of Sciences, Urumqi 830011, China.
[2] Center of Materials Science and Optoelectronics Engineering, University of Chinese Academy of Sciences, Beijing 100049, China.
✉ Corresponding author. E-mail: zhangbocas@ms.xjb.ac.cn

Received: April 26, 2025; Revised: July 26, 2025; Accepted: August 16, 2025

microwave dielectric-thermosensitive multifunctional ceramics has significant potential.

Spinel oxides (AB_2O_4) have become a focal point in the field of materials research because of their multifunctional properties for optical, electrical, magnetic, and catalytic applications [13–16]. Recent studies have extended their applications to microwave dielectrics because of their inherent low dielectric constant (ε_r < 10) and small loss tangent (tanδ < 0.001), which are essential for high-frequency communication systems. Within this family, $MgAl_2O_4$, which has a cubic spinel structure, is the most representative. Shannon *et al.* [17] first reported the dielectric properties of $MgAl_2O_4$ single-crystal ceramics measured at 1 MHz in 1991, with ε_r = 8.325 and tanδ = 0.0008. By 2005, Sebastian and colleagues succeeded in obtaining $MgAl_2O_4$ ceramics with excellent microwave dielectric properties (ε_r = 8.8, $Q{\cdot}f$ = 68,900 GHz, and $\tau_f = -75\times10^{-6}$ °C^{-1}) [18], which surpassed their previously reported $ZnAl_2O_4$ ceramic (ε_r = 8.5, $Q{\cdot}f$ = 56,300 GHz, and $\tau_f = -79\times10^{-6}$ °C^{-1}) [19]. Notably, owing to its high-temperature stability and ultrawide bandgap, $MgAl_2O_4$ is expected to serve as a high-temperature thermistor following ion doping or composite engineering [20,21]. Through such strategies, the inherent dielectric properties can synergize with the thermal sensitivity, enabling the realization of microwave dielectric-thermosensitive multifunctional ceramics.

Previous studies have shown that achieving complete densification through composite modification is difficult [22]. Therefore, solid solution modulation is an excellent strategy for achieving property integration while maintaining structural integrity [23]. $MnFe_2O_4$ shares the same $Fd\bar{3}m$ space group as $MgAl_2O_4$ and generally has an inverse-spinel or semi-inverse-spinel structure [24]. Studies have further demonstrated that $MnFe_2O_4$ has low ε_r and tanδ values, suggesting its potential for use in microwave dielectric applications [25]. Moreover, the valence transitions of Mn/Fe ions under external stimuli result in the formation of mixed valence states of Mn^{2+}/Mn^{3+} and Fe^{2+}/Fe^{3+}, implying their suitability as NTC thermistor materials due to their enhanced electrical conductivity. On the basis of the small polaron hopping model, the conductivity can be attributed to electron hopping between variable valence states of the cations [26]. However, $MgAl_2O_4$ is unsuitable for thermistors due to its high resistivity, while $MnFe_2O_4$ suffers from poor stability and low resistivity, precluding high-temperature applications. Hence, our previous work [8] took advantage of this structural consistency to prepare $Mg_xMn_{1-x}Al_{2x}Fe_{2(1-x)}O_4$ ceramics by solid solution modulation. When x = 0.8, the $Mg_{0.8}Mn_{0.2}Al_{1.6}Fe_{0.4}O_4$ ceramic has a high B ($B_{100/1100°C}$ = 8056 K) value and the lowest aging coefficient, which is expected to provide accurate temperature measurements over a wide temperature range and in the high-temperature region. However, non-Arrhenius behavior persists in the electrical properties above 700 °C (coefficient of determination for lnρ and 1000/T (R^2) < 0.98), resulting from charge equilibrium disruption induced by B-site metastable ion migration. This phenomenon occurs when variable-valence ions are present in the spinel structure [27,28] and represents a key challenge requiring resolution.

The 4f-electron configuration of rare-earth elements dictates their unique atomic structures and physicochemical characteristics, endowing them with distinctive optical, electrical, magnetic, and thermal attributes. As a result, rare-earth ion modifications play critical roles in microstructure evolution, lattice stabilization, and dielectric behavior. Although the more commonly used rare-earth elements are Nd, Y, Sm, Ce, and Sc have important roles in stabilizing the crystal structure of solid oxide electrolytes and modulating ion mobility [29,30]. Building upon this rationale, we designed a series of $Mg_{0.8}Mn_{0.2}Al_{1.6-x}Sc_xFe_{0.4}O_4$ (x = 0–0.4, denoted ySc-MMAFO where $y = 10x$) via B-site substitution, with $Mg_{0.8}Mn_{0.2}Al_{1.6}Fe_{0.4}O_4$ as the substrate. The crystal structures, microstructures, thermosensitive properties, and microwave dielectric properties of the ceramics were also fully characterized and analyzed. As expected, Sc^{3+} substitution effectively addressed the problem of poor linearity due to the variation in B values in the high-temperature range, and excellent microwave dielectric properties were also obtained. Importantly, the 3Sc-MMAFO ceramic was designed into cylindrical dielectric resonator antennas (CDRAs) via CST Microwave Studio 2019 simulation software, and prototype CDRAs were fabricated to realize Ku-band satellite communication applications. Ultimately, Sc^{3+}-modified Mg–Al–Mn–Fe–O spinel ceramics synergistically optimize the microwave dielectric and thermosensitive properties, which provide a pathway to advance multifunctional integration strategies for 6G communication front-end systems.

2 Experimental methods

Multifunctional ySc-MMAFO (y = 1–4) ceramics were synthesized via a conventional solid-state reaction method. The detailed synthesis procedures (shown in Fig. S2 in the ESM) were reported in our previous study [8]. In this study, the sintering temperature of the ceramics was 1510 °C. The structures of the ceramics were characterized by an X-ray diffractometer (XRD; D8-Advance, Bruker, Germany) using Cu Kα radiation in the 2θ range from 0° to 90° with a scanning speed of 0.2 (°)/s. The Raman spectra were recorded at room temperature (RT) via a LabRAM HR Evolution confocal Raman microscope (Horiba, France). The phase information was analyzed via Rietveld refinement of the XRD patterns using GSAS-II software. The microstructure and composition of the sintered pellets were observed by a scanning electron microscope (SEM; SUPRA 55 VP, Zeiss, Germany) in combination with an energy dispersive spectrometer (EDS; Nano GmbH Berlin, Bruker, Germany). The grain size was measured using the intercept method, and the number of tested grains was greater than 100. A cross-section of a ceramic sample for electron microscopy was prepared by focused ion beam (FIB) thinning. High-resolution transmission electron microscopy (HRTEM) of the samples was performed via a transmission electron microscope (TEM; JEOL, JEM-2100F, Japan). The chemical state of the as-sintered pellets was determined via an X-ray photoelectron spectrometer (XPS; Thermo Scientific, Escalab 250Xi, USA) with Al Kα radiation at RT. The XPS results of all elements were calibrated against the standard C 1s peak. The XPS data were analyzed through Gaussian–Lorentzian curve fitting, where the parameters were optimized such that the fitting function was closest to the actual energy spectrum curve. An electron paramagnetic resonance spectrometer (EPR; Bruker D300, Germany) was used to detect the presence of oxygen vacancies on the surface of the material.

To measure the electrical properties, the parallel faces of the sintered samples were coated with platinum paste and then annealed at 900 °C for 30 min. Direct-current (DC) resistance measurements were conducted from 200 to 1000 °C via a Fluke 2638A data acquisition system coupled with a Fluke 9150 furnace and Fluke 1586A multiplexer (USA). The material constant B and sensitivity coefficient (α_T) can be calculated via Eqs. (1) and (2):

$$B = \frac{\ln(\rho_1/\rho_2)}{1/T_1 - 1/T_2} \tag{1}$$

$$\alpha_T = -\frac{B}{T^2} \tag{2}$$

where ρ_1 and ρ_2 are the resistance values at the absolute temperatures of T_1 and T_2, respectively, and T is the absolute temperature (in Kelvin). Impedance spectroscopy was measured

via an impedance analyzer (E4980AL, Keysight, USA) over a frequency range of 20 Hz–1.78 MHz and a temperature range of 25–1200 °C. The microwave dielectric properties (ε_r, $Q{\cdot}f$) were evaluated via the $TE_{01\delta}$ ($TE_{01\delta}$ refers to a specific electromagnetic resonance mode in dielectric resonators) resonant mode method with a vector network analyzer (E5063A, Keysight, USA). The resonance frequency was measured at various temperatures, and Eq. (3) was used to calculate τ_f of the ceramics:

$$\tau_f = \frac{f_{85} - f_{25}}{f_{25}(85-25)} \times 10^{-6} \quad (3)$$

where f_{85} and f_{25} correspond to the resonant frequencies measured at temperatures of 85 and 25 °C, respectively. CDRA was designed and simulated via CST Microwave Studio 2019 simulation software. To evaluate the performance of the antenna, the reflection parameters S_{11} were measured via a microwave network analyzer. The experimental procedures were outlined as follows: the ground plate material was the Rogers RT5880 substrate, characterized by $\varepsilon_{r,sub}$ = 2.20 and tanδ = 0.0009. Additionally, metallic copper was employed as the electrode material on the substrate, with electrode structures fabricated via printed circuit board technology. The CDRA was fabricated from $Mg_{0.8}Mn_{0.2}Al_{1.3}Sc_{0.3}Fe_{0.4}O_4$ ceramics through wire-cutting of simulation-optimized geometries, and subsequently bonded to the center of the metal ground plate by conductive epoxy.

3 Results and discussion

3.1 Design of $Mg_{0.8}Mn_{0.2}Al_{1.6}Fe_{0.4}O_4$-based multifunctional ceramics

3.1.1 *Crystal structure analysis*

Figure 1(a) shows the XRD patterns of the *y*Sc-MMAFO ceramics. The main phase corresponds to the spinel structure of $MgAl_2O_4$ in the $Fd\bar{3}m$ space group. A Sc_2O_3 secondary phase (PDF#05-0629) emerges at $x \geq 0.02$, attributed to the limited solubility of Sc^{3+} in the spinel lattice and complex sintering kinetics. To explore the internal structural features in detail, Rietveld refinement was performed on a representative 3Sc-MMAFO ceramic, as depicted in Fig. 1(b) (the results for the other samples are displayed in Fig. S3 and Table S1 in the ESM). The refined confidence coefficients (R_{wp}) are less than 10%, and the χ^2 values are small, confirming that the results are reliable. Figure 1(c) presents the crystallographic framework of the ceramic sample. This structure comprises a continuous network of tetrahedral and octahedral units that form the primary lattice. Variable valence ions can be located in both the A and B sites of the spinel, and Sc^{3+} can only occupy the octahedral B site. Therefore, its chemical formula can be written as $[Mg_{0.8}Mn_{0.2-i}Fe_i]_{tetra}[Al_{1.6-x}Sc_xMn_iFe_{0.4-i}]_{oct}O_4$ (where i denotes the degree of spinel inversion). As shown in Fig. 1(d), the lattice parameters linearly expand with increasing Sc^{3+} concentration y ($a = b = c$: 8.082 → 8.117 Å; V: 527.8 → 535.1 Å^3), following Vegard's law [31]. This monotonic expansion directly correlates with the larger ionic radius of Sc^{3+} (0.745 Å) than that of Al^{3+} (0.535 Å).

3.1.2 *Raman spectral analysis*

Compared with XRD, Raman spectroscopy is more sensitive to short-range structural distortions. The deconvoluted Raman spectrum in the range of 100–870 cm^{-1} shown in Fig. 1(e) was fitted via a Gaussian–Lorentzian function, resolving five eigenmodes consistent with the group theory prediction for $Fd\bar{3}m$ spinel: $\Gamma_{Raman} = E_g + A_{1g} + 3T_{2g}$ (where the $3T_{2g}$ mode is labeled T^1_{2g}, T^2_{2g}, and T^3_{2g} on the basis of wavenumber) [32,33]. High-frequency modes (> 650 cm^{-1}) originate from symmetric A/B–O stretching vibrations within octahedral [A/BO$_6$] units [34], whereas mid-range modes (300–650 cm^{-1}) arise from asymmetric

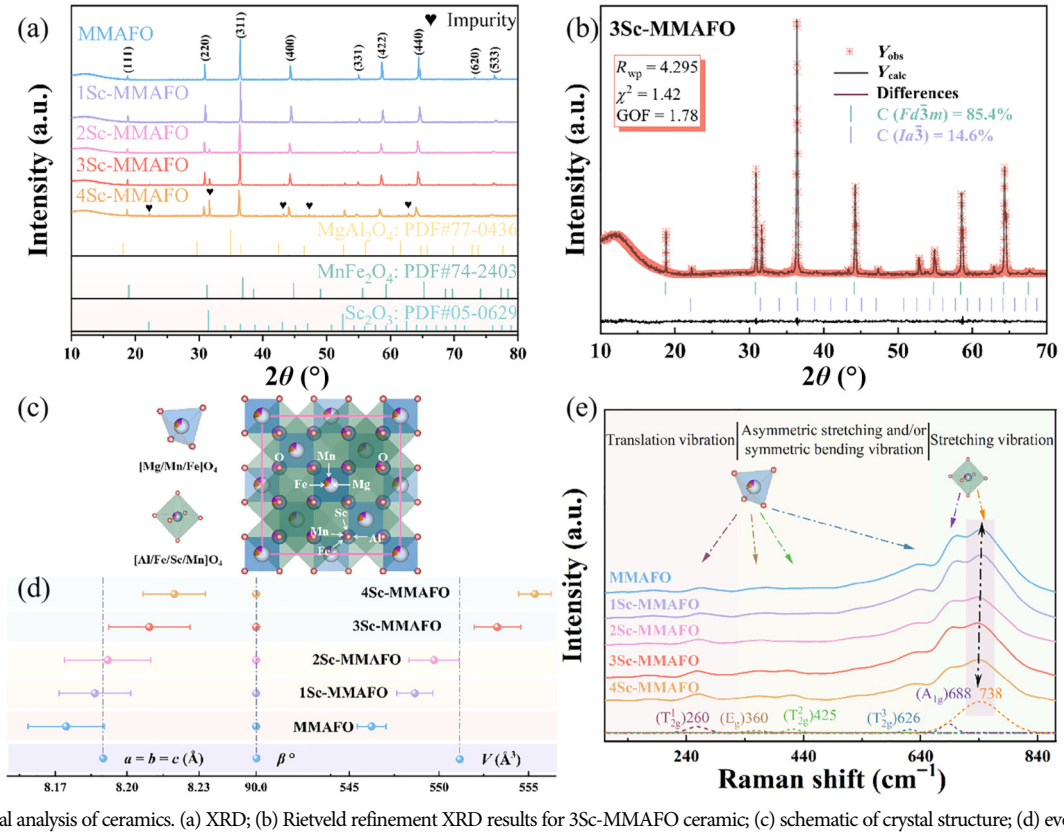

Fig. 1 Structural analysis of ceramics. (a) XRD; (b) Rietveld refinement XRD results for 3Sc-MMAFO ceramic; (c) schematic of crystal structure; (d) evolution of lattice constants as a function of *y*; (e) Raman spectra.

stretching/bending in tetrahedral [A/BO_4] sites [32,35]. Low-frequency modes (< 300 cm^{-1}) are assigned to translational motions of tetrahedral units [36]. The broad asymmetric bands in the E_g and A_{1g} modes are typical of synthetic spinels [37]. Furthermore, the observed redshift of the A_{1g} mode (Fig. 1(e)) directly confirms lattice expansion. This phenomenon arises from the increased interatomic bond lengths induced by lattice expansion, which drives the crystal lattice into a more relaxed state, thereby reducing the vibrational frequency and ultimately attenuating the Coulombic interactions between cations and anions [32].

3.1.3 *Density and microstructure analysis*

The theoretical density (ρ_{theo}) was calculated via crystallographic parameters (Eq. (4)):

$$\rho_{theo} = \frac{Z \times A}{V_{cell} \times N_A} \quad (4)$$

where A, Z, N_A, and V_{cell} denote the molar mass, number of cells per molecule, Avogadro constant, and unit cell volume, respectively. The relative density (ρ_r) of the sample is the ratio of its bulk density ρ_{bulk} to ρ_{theo} and is given by Eq. (5):

$$\rho_r = \frac{\rho_{bulk}}{\rho_{theo}} \quad (5)$$

All samples exhibit high relative densities (> 98%) (Fig. S4(f) in the ESM), implying that density, porosity, and grain size have negligible effects on the quality, which plays an important role in reducing tanδ (enhancing the $Q{\cdot}f$ values). Furthermore, SEM images of the polished and thermally etched ceramic surfaces are shown in Figs. S4(a)–S4(e) in the ESM, revealing uniform grains, relatively well-defined grain boundaries, and a few visible pores. Residual porosity arises from oxygen evolution during solid-state synthesis, as evidenced by the redox reaction: $1.6MgO + (1.6-x)Al_2O_3 + 0.4MnO_2 + 0.4Fe_2O_3 + xSc_2O_3 \rightarrow 2Mg_{0.8}Mn_{0.2}Al_{1.6-x}Sc_xFe_{0.4}O_4 + 0.4O_2$. Sc^{3+} substitution induces significant grain refinement, with the average grain size decreasing from 12.86 μm (y = 0) to 2.47 μm (y = 4) (Figs. S4(a)–S4(e) in the ESM). The tunability of the grain size proves that Sc^{3+} is an effective microstructure modifier and provides a controllable substitution strategy for performance optimization.

A comprehensive microstructural characterization of the sample with y = 3 was conducted through correlated HRTEM and selected-area electron diffraction (SAED) analyses. As shown in Fig. 2(a), there is atomic-scale agreement between the refined XRD structural model projected along the axis of the [211] region and the inverse fast Fourier transform (IFFT) image of the HRTEM region. Small amounts of the secondary phase Sc_2O_3 are present but have little effect on the structure. Notably, the IFFT-processed image in Fig. 2(c) shows contrast undulations, indicating the presence of localized lattice distortions in the ceramic matrix. The normal strains along the xx and yy directions were derived from geometric phase analysis (GPA) calculations, which revealed that compressive strains were accompanied by a small amount of symmetric tensile–compressive strains (Figs. 2(d) and 2(e)). The quantitative results (as shown in Fig. S5 in the ESM) indicate that the compressive strain is significantly greater than the tensile strain, which is related to the lattice expansion due to greater cation substitution. The HRTEM image (Fig. 2(f)) shows clear lattice fringes with a measured facet spacing of approximately 2.8 Å, indexed to the (022) plane for the 3Sc-MMAFO ceramic. The absence of diffraction spot splitting in the SAED pattern of Fig. 2(g) further confirms the excellent crystallinity of the material. EDS elemental mapping (Fig. 2(i)) revealed a homogeneous distribution of Mg, Mn, Al, Sc, and Fe at submicron scales, confirming the chemical homogeneity of the solid solution.

3.1.4 *XPS analysis*

Figure 3 presents the XPS spectra of Fe 2p, Mn 2p, O 1s, and Sc 2p. Fitting the XPS spectra with a Gaussian–Lorentzian function revealed that the binding energies of Fe^{2+}, Fe^{3+}, Mn^{2+}, and Mn^{3+} are within the ranges of 710.11–710.58, 711.78–712.54, 640.43–640.92, and 641.60–642.44 eV, respectively. In addition, the positions of the XPS peaks of all the characteristic elements shifted with increasing Sc^{3+} substitution. This is mainly due to the change in the binding energy required to form a stable lattice, which is also the second phase of Sc_2O_3. Notably, as the degree of Sc^{3+} substitution increases, the Fe 2p, Mn 2p, and O 1s XPS peaks shift to the left at first and then gradually shift to the right, which means that Sc^{3+} substitution increases the binding energy when y = 1. This is because at this point, the lattice mismatch is at its

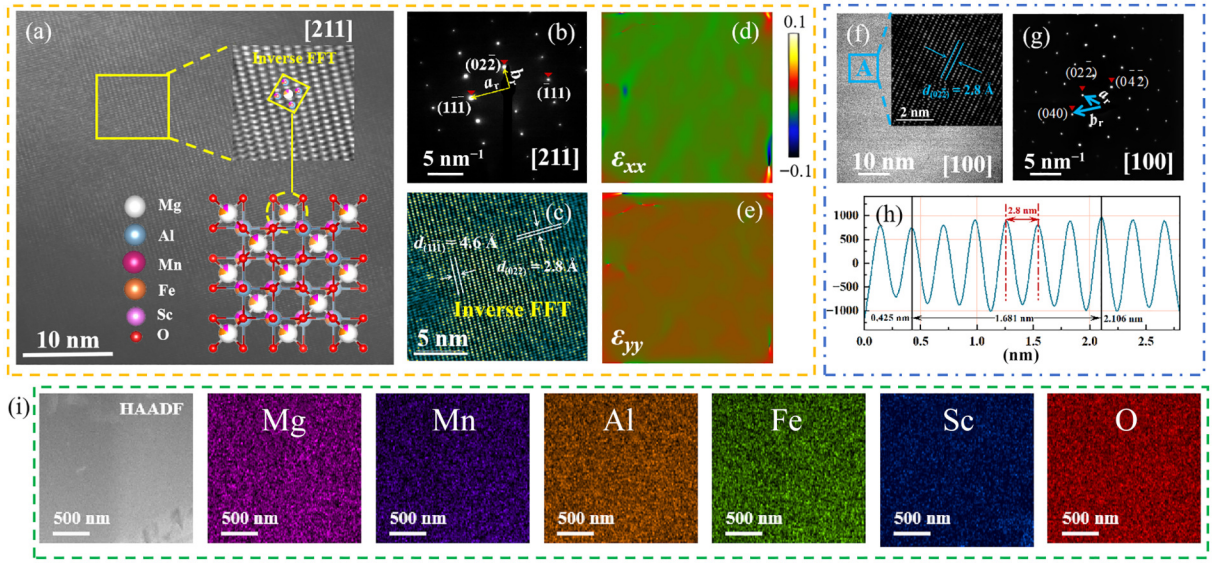

Fig. 2 Microstructural analysis of 3Sc-MMAFO ceramic. (a) HRTEM image and crystal structure viewed along [211] zone axis; (b) SAED pattern; (c–e) IFFT and GPA analyses. (f, g) HRTEM image and SAED image along [100] zone axis; (h) lattice fringe spacing from the blue box in (f); (i) EDS elemental mappings.

maximum, but as the Sc^{3+} substitution level gradually increases, the lattice mismatch gradually decreases as the secondary phase Sc_2O_3 separates, which leads to a decrease in the binding energy. The Sc 2p XPS peaks are significantly shifted to the right, which means that the binding energy reaches its maximum when $y = 1$ and then decreases because of the precipitated Sc_2O_3. To analyze the oxygen vacancy concentration quantitatively, peak deconvolution of the O 1s XPS spectrum was performed. The O 1s peak of *y*Sc-MMAFO was resolved into three components corresponding to lattice oxygen (O_L), oxygen vacancies (O_V), and surface adsorbed oxygen (O_A). Quantitative analysis revealed a decrease in the oxygen vacancy concentration from 25.71% to 16.58%. To verify the presence of oxygen vacancies and their variation trends, the samples were characterized by electron paramagnetic resonance (EPR). As shown in Fig. 3(e), the EPR signal intensity at g = 2.0033 progressively attenuated with increasing substitution content, confirming a reduction in the concentration of oxygen vacancies. This trend was further corroborated by low-temperature EPR measurements (Fig. S6 in the ESM).

3.2 NTC thermistor properties

The impedance spectrum (IS) of the *y*Sc-MMAFO ceramics was measured over the temperature range of 323–773 K (Figs. 4(a) and 4(b) and Fig. S7(a) in the ESM). Notably, the Nyquist plots reveal three distinct impedance contributions: (1) a high-frequency intercept on the real impedance axis (Z') (inset of Fig. 4(a)), corresponding to the grain resistance (R_g); (2) semicircular arcs in the mid-frequency range, reflecting the grain boundary resistance (R_{gb}); (3) low-frequency arcs associated with electrode effects [38,39]. To analyze the high-frequency and low-frequency response characteristics more intuitively, we extracted R_g, R_{gb}, and the grain-boundary capacitance (Fig. S9 and Table S2 in the ESM) via the equivalent circuit model shown in Fig. S8 in the ESM. In the imaginary impedance Z''–f spectra, the broadening of the Z'' peak profile with increasing temperature indicates the presence of a temperature-dependent dielectric relaxation mechanism (Fig. S7(b) in the ESM) [40].

The resistance–temperature curves exhibit typical NTC behavior (shown in Fig. S7(c) in the ESM). All the samples show a consistent decrease in resistance as the temperature increases. The relationship between the natural logarithm of the resistivity ($\ln\rho$) and the reciprocal of the absolute temperature ($1000/T$) conforms to the Arrhenius equation (Fig. 4(c)), which can be described by Eq. (6) [41]:

$$\rho = \rho_0 \exp(B/T) = \rho_0 \exp(E_a/(kT)) \quad (6)$$

where ρ_0 is the resistivity at infinite temperature ($T \to \infty$); T is the absolute temperature; E_a is the activation energy for electrical conduction and can be calculated from the slopes of the $\ln\rho$–$1000/T$ plots; k is the Boltzmann constant. As shown in Fig. 4(c), Sc^{3+} substitution significantly increases the slope of $\ln\rho$–$1000/T$, which also indicates an increase in the hopping activation energy (E_a), as shown in Fig. 4(d). In this regard, the substitution of Sc^{3+} has a similar effect to the addition of other nonconductive ions, which essentially increases the difficulty of hopping small polarons [42,43].

Resistivity and the B value are significant parameters affecting NTC thermistor properties. Resistivity imposes no strict constraints, as device resistance can be geometrically tailored [44]. The B value, however, critically governs the thermistor sensitivity. This sensitivity is quantified by the temperature coefficient of resistance (α_T), which is defined by Eq. (2) and is directly proportional to the B value and has an inverse quadratic relationship with the temperature (T). Notably, α_T decreases significantly with increasing temperature. Consequently, achieving high sensitivity at elevated temperatures necessitates materials with high B values.

Figure 4(d) shows the B values of all the samples. The B values of the Sc^{3+}-doped samples are significantly greater than those of the unmodified samples. On the basis of the analysis of the XPS data, the substitution of Sc^{3+} promoted the oxidation of Mn^{2+} to Mn^{3+} and the reduction of Fe^{3+} to Fe^{2+}. The significant change in the ionic valence ratio leads to an increase in the activation energy of the polaron hopping, which in turn induces a synergistic increase in the resistivity and B values. The B values of the *y*Sc-MMAFO ceramics over the corresponding temperature ranges

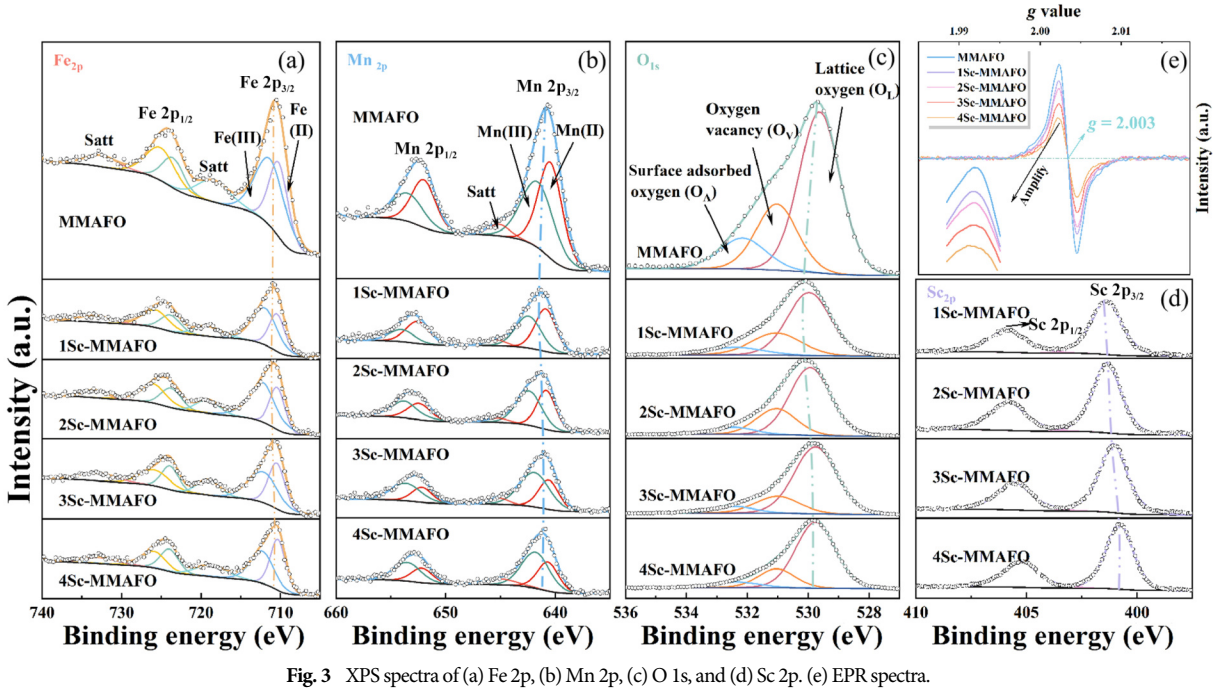

Fig. 3 XPS spectra of (a) Fe 2p, (b) Mn 2p, (c) O 1s, and (d) Sc 2p. (e) EPR spectra.

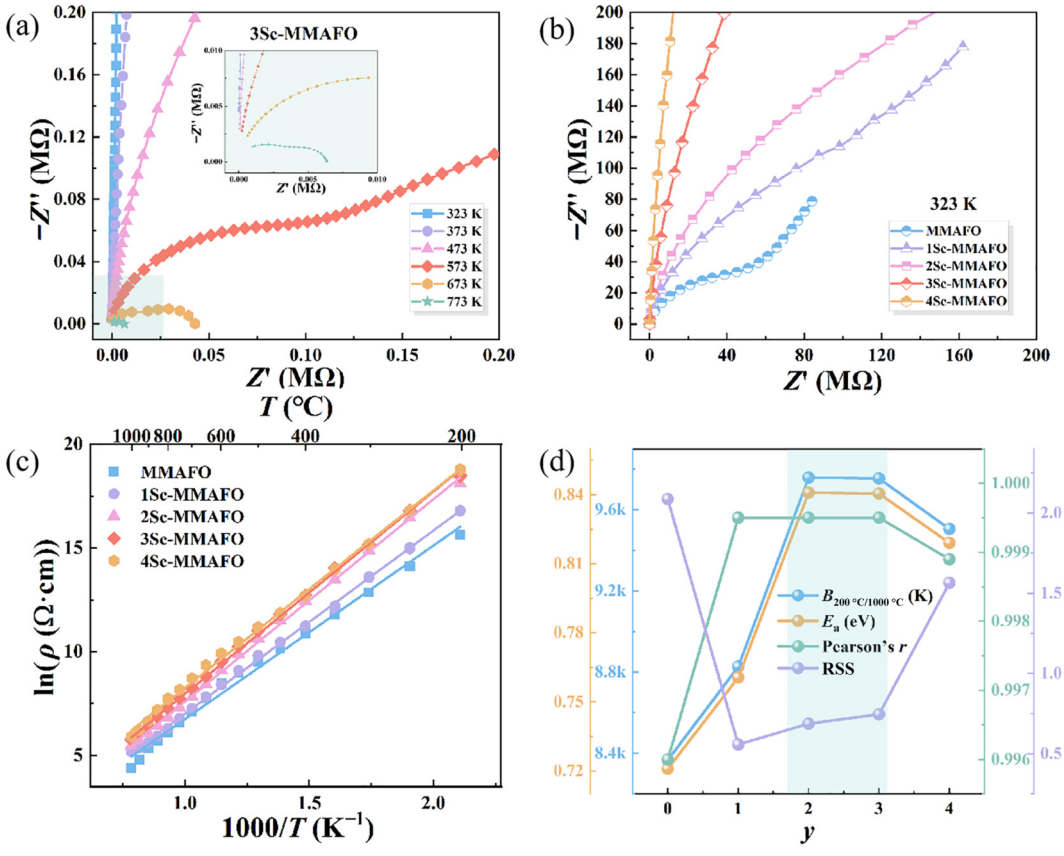

Fig. 4 NTC thermistor properties of ceramics. (a) IS of 3Sc-MMAFO ceramic measured between 323 and 773 K; (b) IS at 323 K; (c) relationship between lnρ and 1000/T; (d) linear fitting parameters: B, E_a, r, and RSS.

were calculated (Fig. S7(d) in the ESM). Notably, the 2Sc-MMAFO and 3Sc-MMAFO ceramics not only have a wider operating temperature range (200–1000 °C) but also higher B values (9758 and 9754 K) than the undoped sample does, ensuring a wider temperature range and higher temperature sensitivity. In addition, the linearity of the lnρ–1000/T curves for the Sc^{3+}-substituted samples was significantly improved and optimized. Pearson's r increases from 0.9960 to 0.9995. For samples with y = 2 and 3, the relationship between lnρ and 1000/T maintains excellent linearity even at temperatures as high as 1000 °C. These findings emphasize the efficacy of Sc^{3+} substitution in improving the linearity of thermistor materials.

3.3 Low-frequency dielectric behavior

To investigate the dielectric behavior of the ceramics, low-frequency dielectric measurements were systematically conducted over a wide temperature range of 25–400 °C, as shown in Fig. S10 in the ESM. As shown in Fig. 5(a), the ε_r curves of all the samples are approximately parallel to the x-axis (below 200 °C), indicating good stability of ε_r. In the low-frequency range, the tanδ values remain below 0.016, among which the 3Sc-MMAFO sample has a minimal tanδ of 0.0013 under the measurement conditions of 1 MHz and 50 °C.

Figure 5(b) shows the variation in ε_r with frequency at RT. ε_r decreases rapidly at low frequencies and finally reaches a constant frequency-independent point at 1 MHz, exhibiting typical dielectric behavior. This frequency-dependent behavior stems from the different contributions of the four polarization mechanisms in the material. At low frequencies, electron displacement, ion displacement, dipole orientation, and space–charge polarization collectively dominate the total polarization [45]. With increasing frequency, however, the relaxation processes associated with defect dipoles and space–charge polarization can no longer follow the rapid variations in the applied electric field. Consequently, high-frequency polarization is governed solely by electron and ion displacement mechanisms [46]. Figure 5(b) also depicts the frequency dependence of tanδ. Oxygen vacancies generate space charges that form leakage currents at grain boundaries, leading to elevated tanδ values at low frequencies. As the frequency increases, these charges cannot keep pace with the reversal of the applied electric field, resulting in a tendency toward lower saturation values [47].

3.4 Microwave dielectric properties

3.4.1 *Dielectric constant*

As shown in Fig. 5, ε_r gradually increases with the substitution of Sc^{3+} with high ionic polarizability ($\alpha(Sc^{3+})$ = 2.81 Å^3 vs. $\alpha(Al^{3+})$ = 0.79 Å^3). The ε_r of ceramics depends on internal factors (ionic polarizability and lattice vibration) as well as external factors (density and phase composition) [48,49]. To eliminate the effect of porosity on the ε_r of ySc-MMAFO ceramics, a correction formula was applied via Bosman and Havinga's correction formula, as shown in Eqs. (7) and (8):

$$\varepsilon_{cor} = \varepsilon_r(1 + 1.5P) \tag{7}$$

$$P = 1 - \rho_r \tag{8}$$

where ε_{cor} is the corrected dielectric constant, and P is the porosity percentage. In addition, to investigate the relationship between the dielectric constant and polarizability of materials, researchers have

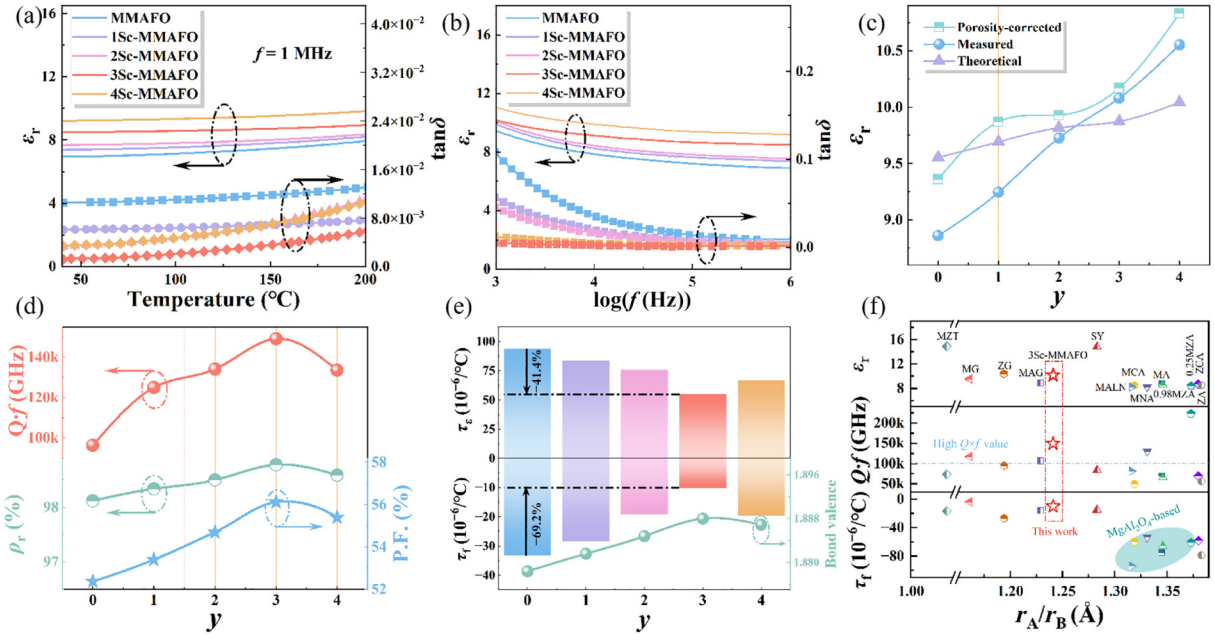

Fig. 5 Microwave dielectric properties of *y*Sc-MMAFO ceramics. (a) Temperature dependence of ε_r and tanδ at 1 MHz; (b) frequency dependence of ε_r and tanδ at RT; (c) dielectric constant: ε_r, ε_{cor}, and ε_{theo}; (d) $Q{\cdot}f$, ρ_r, and PF; (e) τ_f and τ_ε; (f) comparison of microwave dielectric properties of spinel-type ceramics, where r_A and r_B denote the equivalent ionic radii of the A-site and B-site, respectively.

proposed the concept of the theoretical dielectric constant (ε_{theo}) and calculated the value of ε_{theo} via the Clausius–Mosotti equation (Eq. (9)):

$$\varepsilon_{theo} = \frac{3V_m + 8\pi\alpha}{3V_m - 4\pi\alpha} \tag{9}$$

where V_m is the molecular volume, and α is the polarizability of the *y*Sc-MMAFO ceramics. The total ionic polarizability of *y*Sc-MMAFO was predicted via Eq. (10):

$$\alpha_{theo} = \alpha(Mg^{2+}) + \alpha(Mn^{2+}) + (1-x)\alpha(Al^{3+}) + x\alpha(Sc^{3+}) + \alpha(Fe^{3+}) + 4\alpha(O^{2-}) \tag{10}$$

where $\alpha(Mg^{2+})$, $\alpha(Mn^{2+})$, $\alpha(Al^{3+})$, $\alpha(Sc^{3+})$, $\alpha(Fe^{3+})$, and $\alpha(O^{2-})$ are the ion polarizability values and can be obtained via the Shannon method [50] (as shown in Table S1 in the ESM). The calculated porosity-corrected and theoretical dielectric constants are shown in Fig. 5(c), which are consistent with the trends of the measured values. The small deviation between the theoretical and measured dielectric constants arises from the fact that the ion polarizability used in the calculations is an empirical parameter. Notably, the porosity-corrected ε_{cor} exceeds the measured values, which is attributed to the presence of pores in the actual microstructure, lowering the dielectric constant. The analysis demonstrated the dominant role of porosity (or density) in the macroscopic dielectric response of ceramics.

3.4.2 $Q{\cdot}f$

Figure 5(d) shows the variation in $Q{\cdot}f$, the packing fraction (PF), and the relative density as a function of the concentration of Sc^{3+}. The PF is mainly used to describe cell space utilization, which is often considered a major factor affecting the Q value of microwave dielectric ceramics. Kim *et al.* [51] concluded that a higher PF leads to weaker vacancy scattering inside the crystal, which reduces loss in the system. Structural and atomic data were obtained for the samples through Rietveld refinement, from which PF was calculated via Eq. (11):

$$PF = \frac{\frac{4\pi}{3} \times (r^3_{(Mg/Mn)} + 2r^3_{(Al/Sc/Fe)} + 4r^3_O) \times Z}{V_{cell}} \tag{11}$$

where $r_{(Mg/Mn)}$, $r_{(Al/Sc/Fe)}$, r_O, and V_{cell} are the effective ionic radii at each coordination number and the unit cell volume, respectively. The experimental data reveal a strong positive correlation between PF and $Q{\cdot}f$, peaking simultaneously at $y = 3$ with PF = 56.12% and $Q{\cdot}f$ = 149,000 GHz.

3.4.3 *Temperature coefficient of resonant frequency*

The structural features of the oxygen octahedron significantly affect the τ_f value. It is evident from Fig. 1(d) and Table S1 in the ESM that the unit cell volume increases and the average bond length of the Mn/Al/Sc/Fe–O bond decreases with increasing *y*. The change in bond length leads to a change in bond valence, and an increase in the bond valence at the B site usually leads to a decrease in the value of $|\tau_f|$, which is calculated via Eqs. (12) and (13) [52]:

$$V_{ij} = \sum_j^i v_{ij} \tag{12}$$

$$v_{ij} = \exp\left(\frac{R_{ij} - d_{ij}}{b'}\right) \tag{13}$$

where R_{ij} is the bond valence parameter, d_{ij} denotes the bond length between two atoms, and b' is a constant of 0.37 Å. Figure 5(e) shows that the value of τ_f follows the opposite trend of the bond valence. This is due to the increase in the lattice energy and tilt-restoring force of the oxygen octahedron with increasing bond valence, thus leading to a decrease in $|\tau_f|$.

Moreover, τ_f is related to the temperature coefficient of the dielectric constant (τ_ε) and the linear coefficient of thermal expansion (α_L) [53]:

$$\tau_f = -\left(\frac{\tau_\varepsilon}{2} + \alpha_L\right) \tag{14}$$

The α_L values of all the Sc^{3+}-substituted ceramics are close (as shown in Fig. S11 in the ESM), suggesting that τ_ε plays a key role in regulating the magnitude of τ_f. The same tendency for τ_ε and τ_f can be seen in Fig. 5(e).

3.4.4 *Comparison of the microwave dielectric properties*

Figure 5(f) shows the microwave dielectric properties of some spinel-type ceramics as a function of the ionic radius ratio at the A/B sites [18,19,54–65]. These spinel materials usually have low relative dielectric constants and high-quality factors, which are potentially valuable for applications in millimeter-wave signal propagation. The dielectric constants of the $MgAl_2O_4$-based ceramics are basically stable in the range of 8–10, indicating that their properties are independent of the ionic radius. Compared with $MgAl_2O_4$, the designed 3Sc-MMAFO ceramics have superior microwave dielectric properties (ε_r =10.08, $Q{\cdot}f$= 149,000 GHz, and τ_f = -10.2×10^{-6} °C^{-1}). These findings indicate that Sc^{3+} ion substitution is an effective way to improve the microwave dielectric properties of $MgAl_2O_4$-based dielectric ceramics, which makes the developed dielectric ceramics promising for application in 5G/6G communication devices.

3.5 Design of CDRA

To validate the potential of ceramics for high-frequency applications, a 3Sc-MMAFO-based CDRA was developed, with the structural configuration and critical geometrical parameters detailed in Fig. 6(b). As depicted in Fig. 6(a), this CDRA functions as a millimeter-wave front-end module, achieving high gain, high radiation efficiency, directional beam control, and interference suppression capabilities in signal transmission. The test results indicate a center frequency of 12.01 GHz, bandwidth of 1.8 GHz (11–12.8 GHz), and reflection coefficient (S_{11}) of −35.66 dB (Fig. 6(c)). Operating in the Ku-band (12 GHz), this frequency significantly enhances transmission speed and reliability in satellite communications, mobile wireless networks, and relay transmissions.

The deviation between the simulated and measured values likely originated from manufacturing tolerances and antenna impedance mismatch [66]. The maximum radiation efficiency reaches 92%, with a realized gain of 6.28 dBi (Fig. 6(d)). Figure 6(e) presents the 3D simulated radiation pattern, demonstrating the strongest electromagnetic signal radiation along the *Z* direction. The electric field (*y*-axis polarization) and magnetic field (semicircular distribution in the *xoy*-plane) profiles (Fig. 6(f)) confirm the dominant $HE_{11\delta}$ hybrid mode, which optimizes the broadside radiation in CDRAs. The antenna radiation pattern at 12.01 GHz is shown in Fig. 6(g), where the copolarized field intensity exceeds the cross-polarized intensity along the apparent axis (θ = 0°). The 3Sc-MMAFO CDRA exhibits dual functionality as both a high-Q resonator ($Q{\cdot}f$ = 149,000 GHz) and a high-*B* thermistor sensor ($B_{200/1000°C}$ = 9754 K), enabling self-temperature-compensated RF modules for 6G millimeter-wave massive MIMO base stations.

4 Conclusions

In conclusion, this study presents a systematic study of Mg–Al–Mn–Fe–O spinel ceramics for multifunctional devices. The results demonstrate that the 3Sc–MMAFO ceramic displays NTC thermistor properties across an extended temperature range (200–1000 °C), with a *B* value of 9754 K, ensuring measurement accuracy and temperature sensitivity. In addition, the optimized 3Sc-MMAFO ceramic simultaneously achieves superior microwave dielectric properties with ε_r = 10.08, $Q{\cdot}f$ = 149,000 GHz, and $\tau_f = -10.2\times10^{-6}$ °C^{-1}. Significantly, the developed 3Sc-MMAFO-based resonant antenna demonstrates practical applicability in millimeter-wave systems, operating at 11–

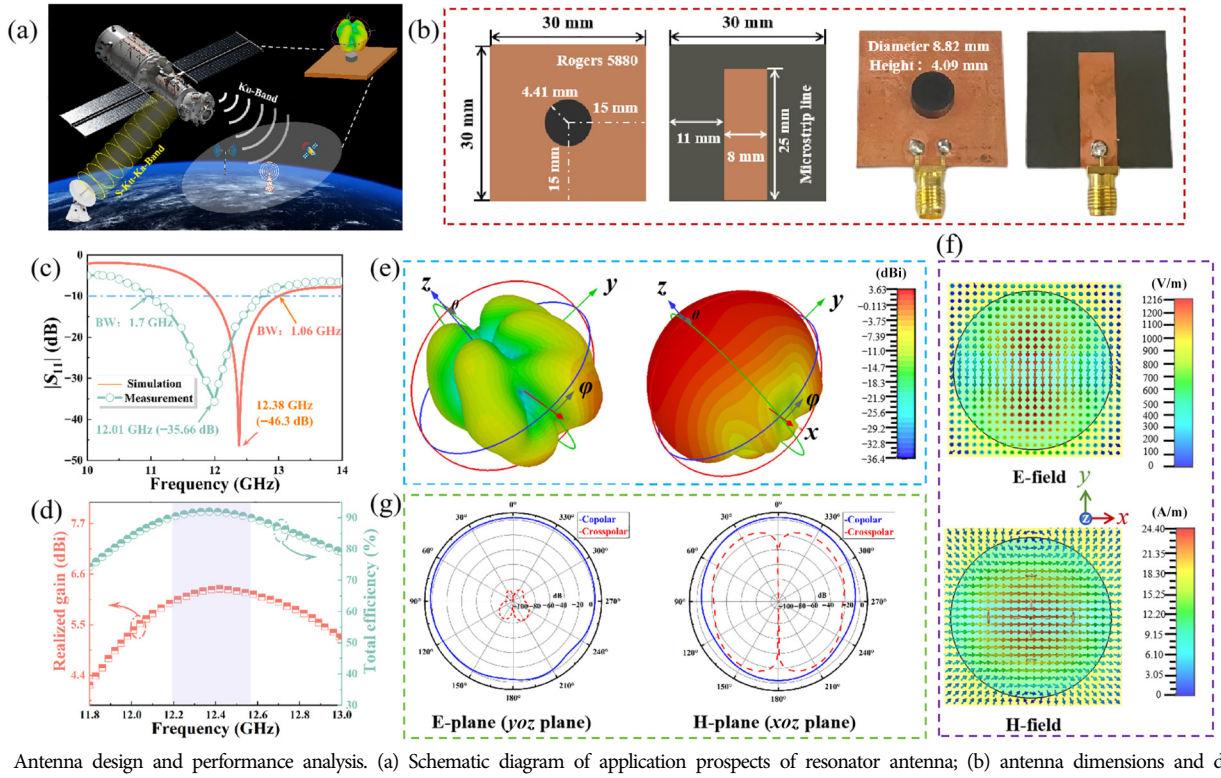

Fig. 6 Antenna design and performance analysis. (a) Schematic diagram of application prospects of resonator antenna; (b) antenna dimensions and design; (c) simulated and measured return loss S_{11} of proposed antenna; (d) simulated antenna radiation efficiency and realized gain; (e) 3D simulated radiation patterns of copolarized and cross-polarized; (f) simulation results of electric field and magnetic field; (g) simulation results of radiation pattern in E and H planes.

12.8 GHz with 92% radiation efficiency and 6.28 dBi realized gain. Ultimately, these comprehensive functional properties establish the 3Sc-MMAFO ceramic as a promising dual-functional material for microwave-thermosensitive integrated devices.

Acknowledgements

We would like to acknowledge financial support from the Natural Science Foundation of Xinjiang Uygur Autonomous Region (No. 2024D01E32), Xinjiang Tianshan Talent Training Program (No. 2023TSYCCX0092), National Natural Science Foundation of China (No. 62471468), and Youth Innovation Promotion Association of CAS (No. Y2023117).

Availability of data and materials

The data that support the findings of this study are available from the corresponding author upon reasonable request.

Competing interests

The authors have no competing interests to declare that are relevant to the content of this article.

Electronic Supplementary Material

Supplementary material is available in the online version of this article at https://doi.org/10.26599/JAC.2025.9221153.

References

[1] Liu K, Zhang DN, Yang YR, *et al.* Sintering behavior, structural evolution, and dielectric properties of $Li_{2+x}MgTiO_4F_x$ microwave dielectric ceramics. *J Eur Ceram Soc* 2023, **43**: 6098–6106.

[2] Mirsaneh M, Leisten OP, Zalinska B, *et al.* Circularly polarized dielectric-loaded antennas: Current technology and future challenges. *Adv Funct Mater* 2008, **18**: 2293–2300.

[3] Synkiewicz-Musialska B, Szwagierczak D, Kulawik J, *et al.* Impact of additives and processing on microstructure and dielectric properties of willemite ceramics for LTCC terahertz applications. *J Eur Ceram Soc* 2020, **40**: 362–370.

[4] He L, Wang JH, Zhang C, *et al.* A spinel-related solid solution ceramic $0.7LiFe_5O_8$–$0.3Li_2MgTi_3O_8$ with high permeability and excellent microwave dielectric properties. *Mater Lett* 2018, **232**: 157–159.

[5] He L, Mi SB, Jin XW, *et al.* Order–disorder phase transition and magneto-dielectric properties of $(1–x)LiFe_5O_8$–$xLi_2ZnTi_3O_8$ spinel-structured solid solution ceramics. *J Am Ceram Soc* 2015, **98**: 2122–2129.

[6] Hao SL, Li JH, Sung QB, *et al.* Improved electrical properties and good thermal luminescent stability of Sm^{3+}-doped $Sr_{1.90}Ca_{0.15}Na_{0.90}Nb_5O_{15}$ multifunctional ceramics. *J Mater Sci—Mater El* 2019, **30**: 13372–13380.

[7] Pan HL, Zhang JJ, Jia XR, *et al.* Large electrostrictive effect and high optical temperature sensing in $Bi_{0.5}Na_{0.5}TiO_3$–$BaTiO_3$–$(Sr_{0.7}Bi_{0.18}Er_{0.02})TiO_3$ luminescent ferroelectrics. *Ceram Int* 2018, **44**: 5785–5789.

[8] Xian Y, Zhou Y, Chen J, *et al.* Modulation of solid solution in $Mg_xMn_{1-x}Al_{2x}Fe_{2(1-x)}O_4$ spinel ceramics for multifunctional devices. *J Am Ceram Soc* 2025, **108**: e20145.

[9] Zhao XM, Chao XL, Wu D, *et al.* Simultaneous realization of high transparency and piezoelectricity in low symmetry KNN-based ceramics. *J Am Ceram Soc* 2019, **102**: 3498–3509.

[10] Zhao XM, Chai QZ, Chen B, *et al.* Improved transmittance and ferroelectric properties realized in KNN ceramics via SAN modification. *J Am Ceram Soc* 2018, **101**: 5127–5137.

[11] Guo WJ, Ma ZY, Luo Y, *et al.* Structure, defects, and microwave dielectric properties of Al-doped and Al/Nd co-doped $Ba_4Nd_{9.33}Ti_{18}O_{54}$ ceramics. *J Adv Ceram* 2022, **11**: 629–640.

[12] Feng C, Zhou X, Tao BJ, *et al.* Crystal structure and enhanced microwave dielectric properties of the $Ce_2[Zr_{1-x}(Al_{1/2}Ta_{1/2})_x]_3(MoO_4)_9$ ceramics at microwave frequency. *J Adv Ceram* 2022, **11**: 392–402.

[13] Zhou ZH, Zhang S, Le YK, *et al.* Defect enrichment in near inverse spinel configuration to enhance the persistent luminescence of Fe^{3+}. *Adv Opt Mater* 2022, **10**: 2101669.

[14] Deepty M, Srinivas Ch, Ranjith Kumar E, *et al.* Evaluation of structural and dielectric properties of Mn^{2+}-substituted Zn-spinel ferrite nanoparticles for gas sensor applications. *Sensor Actuat B—Chem* 2020, **316**: 128127.

[15] Gan GW, Yin YQ, Cheng Y, *et al.* $0.16BaFeO_3$–$0.84MgFe_2O_4$ hexa-spinel composited ferrites with enhanced magneto-dielectric properties for miniaturized high-frequency antennas. *Mater Today Adv* 2024, **22**: 100505.

[16] Xu H, Yuan JJ, He GY, *et al.* Current and future trends for spinel-type electrocatalysts in electrocatalytic oxygen evolution reaction. *Coord Chem Rev* 2023, **475**: 214869.

[17] Shannon RD, Rossman GR. Dielectric constant of $MgAl_2O_4$ spinel and the oxide additivity rule. *J Phys Chem Solids* 1991, **52**: 1055–1059.

[18] Surendran KP, Bijumon PV, Mohanan P, *et al.* $(1–x)MgAl_2O_4$–$xTiO_2$ dielectrics for microwave and millimeter wave applications. *Appl Phys A* 2005, **81**: 823–826.

[19] Surendran KP, Santha N, Mohanan P, *et al.* Temperature stable low loss ceramic dielectrics in $(1–x)ZnAl_4$–$xTiO_2$ system for microwave substrate applications. *Eur Phys J B* 2004, **41**: 301–306.

[20] Yang T, Zhang B, Zhao Q, *et al.* Vacuum hot pressed highly dense, nanograined $Mg(Al_{1-x}Cr_x)_2O_4$ ceramics. *Mater Lett* 2017, **194**: 42–44.

[21] Weeks RA, Sonder E. Electrical conductivity of pure and Fe-doped magnesium–aluminum spinel. *J Am Ceram Soc* 1980, **63**: 92–95.

[22] Zhang B, Zhao Q, Chang AM, *et al.* Spark plasma sintering of $MgAl_2O_4$–$YCr_{0.5}Mn_{0.5}O_3$ composite NTC ceramics. *J Eur Ceram Soc* 2014, **34**: 2989–2995.

[23] Oses C, Toher C, Curtarolo S. High-entropy ceramics. *Nat Rev Mater* 2020, **5**: 295–309.

[24] Zhandun VS, Nemtsev AV. *Ab initio* comparative study of the magnetic, electronic and optical properties of AB_2O_4 (A, B = Mn, Fe) spinels. *Mater Chem Phys* 2021, **259**: 124065.

[25] Murugesan C, Sathyamoorthy B, Chandrasekaran G. Structural, dielectric and magnetic properties of Gd substituted manganese ferrite nanoparticles. *Phys Scripta* 2015, **90**: 085809.

[26] Bhargava A, Eppstein R, Sun JX, *et al.* Breakdown of the small-polaron hopping model in higher-order spinels. *Adv Mater* 2020, **32**: 2004490.

[27] Hao WB, Zhang H, Gao CY, *et al.* Influence of V/Ni-doping on electrical properties and aging stability of $ZnFe_2O_4$-based NTC ceramics. *J Mater Sci—Mater El* 2021, **32**: 17800–17809.

[28] Akhlaghi N, Najafpour-Darzi G. Manganese ferrite ($MnFe_2O_4$) nanoparticles: From synthesis to application-A review. *J Ind Eng Chem* 2021, **103**: 292–304.

[29] Zhu NC, Li RS, Xu SS. Investigation of the semiconductor strained superlattice structure and interface by X-ray rocking-curve analysis. *Acta Phys Sin* 1991, **40**: 433–440.

[30] Arifin NA, Afifi AA, Samreen A, *et al.* Characteristic and challenges of scandia stabilized zirconia as solid oxide fuel cell material—In depth review. *Solid State Ionics* 2023, **399**: 116302.

[31] Magomedov MN. On the deviation from the Vegard's law for the solid solutions. *Solid State Commun* 2020, **322**: 114060.

[32] D'Ippolito V, Andreozzi GB, Bersani D, *et al.* Raman fingerprint of chromate, aluminate and ferrite spinels. *J Raman Spectrosc* 2015, **46**: 1255–1264.

[33] Xie MJ, Lai YM, Liao XY, *et al.* Tunable microware dielectric properties of high-entropy $(Mg_{1/2}Zn_{1/2})_{0.4+x}Li_{0.4}(Co_{1/2}Ni_{1/2})_{0.4-x}Al_2O_4$ ceramics with low loss. *J Materiomics* 2025, **11**: 100894.

[34] Shirai H, Morioka Y, Nakagawa I. Infrared and Raman spectra and lattice vibrations of some oxide spinels. *J Phys Soc Jpn* 1982, **51**: 592–597.

[35] Yamanaka T, Ishii M. Raman scattering and lattice vibrations of Ni_2SiO_4 spinel at elevated temperature. *Phys Chem Miner* 1986, **13**: 156–160.
[36] Álvarez-Docio CM, Reinosa JJ, Del Campo A, *et al*. Investigation of thermal stability of 2D and 3D $CoAl_2O_4$ particles in core–shell nanostructures by Raman spectroscopy. *J Alloys Compd* 2019, **779**: 244–254.
[37] Cynn H, Sharma SK, Cooney TF, *et al*. High-temperature Raman investigation of order–disorder behavior in the $MgAl_2O_4$ spinel. *Phys Rev B* 1992, **45**: 500–502.
[38] Wu RF, Ma MS, Zhang S, *et al*. Enhanced linearity of $CaCu_3Ti_4O_{12}$ by changing energy band structure induced by Fe^{3+} doping for high temperature thermistor application. *Appl Phys Lett* 2022, **121**: 032102.
[39] Zhang P, Lou ZH, Qin MJ, *et al*. High-entropy $(Ca_{0.2}Sr_{0.2}Ba_{0.2}La_{0.2}Pb_{0.2})TiO_3$ perovskite ceramics with A-site short-range disorder for thermoelectric applications. *J Mater Sci Technol* 2022, **97**: 182–189.
[40] Li WJ, Wang J, Poudel B, *et al*. Filiform metal silver nanoinclusions to enhance thermoelectric performance of p-type $Ca_3Co_4O_{9+\delta}$ oxide. *ACS Appl Mater Inter* 2019, **11**: 42131–42138.
[41] Sun H, Wang YF, Liu YF, *et al*. Enhanced thermal stability and broad temperature range in high-entropy $(La_{0.2}Ce_{0.2}Nd_{0.2}Sm_{0.2}Eu_{0.2})NbO_4$ ceramics. *ACS Appl Mater Inter* 2024, **16**: 12821–12832.
[42] Elbadraoui E, Baudour JL, Leroux C, *et al*. Cation distribution, short-range order and small polaron hopping conduction in nickel manganites, from a neutron diffraction study. *Phys Status Solidi B* 1999, **212**: 129–139.
[43] Schmidt R, Basu A, Brinkman AW. Small polaron hopping in spinel manganates. *Phys Rev B* 2005, **72**: 115101.
[44] Liu YF, Wu RF, Sun H, *et al*. High-entropy $CeNbO_{4+\delta}$-based ceramics with ultrahigh comprehensive thermosensitive performances. *ACS Appl Mater Inter* 2024, **16**: 28861–28873.
[45] Li WY, Xian Y, Chang AM, *et al*. New microwave dielectric ceramics based on the $CaRNbWO_8$ (R = Y, La, Ce, Nd or Sm) system. *J Mater Sci—Mater El* 2023, **34**: 1097.
[46] Jonscher AK. Dielectric relaxation in solids. *J Phys D Appl Phys* 1999, **32**: R57.
[47] Narang SB, Kaur D, Bahel S. Dielectric properties of lanthanum substituted barium titanate microwave ceramics. *Mater Lett* 2006, **60**: 3179–3182.
[48] Liao QW, Li LX, Ren X, *et al*. New low-loss microwave dielectric material $ZnTiNbTaO_8$. *J Am Ceram Soc* 2011, **94**: 3237–3240.
[49] Wu FF, Zhou D, Du C, *et al*. Temperature stable $Sm(Nb_{1-x}V_x)O_4$ ($0.0 \le x \le 0.9$) microwave dielectric ceramics with ultra-low dielectric loss for dielectric resonator antenna applications. *J Mater Chem C* 2021, **9**: 9962–9971.
[50] Shannon RD. Dielectric polarizabilities of ions in oxides and fluorides. *J Appl Phys* 1993, **73**: 348–366.
[51] Kim ES, Chun BS, Freer R, *et al*. Effects of packing fraction and bond valence on microwave dielectric properties of $A^{2+}B^{6+}O_4$ (A^{2+}: Ca, Pb, Ba; B^{6+}: Mo, W) ceramics. *J Eur Ceram Soc* 2010, **30**: 1731–1736.
[52] Brese NE, O'Keeffe M. Bond-valence parameters for solids. *Acta Cryst* 1991, **47**: 192–197.
[53] Ma LZ, Jiang LX, Duan JH, *et al*. Enhanced microwave performance in spinel dielectric ceramics using entropy strategy for 5G/6G communication devices. *Chem Eng J* 2025, **503**: 158159.
[54] Yang XZ, Lai YM, Zeng YM, *et al*. Spinel-type solid solution ceramic $MgAl_2O_4$–Mg_2TiO_4 with excellent microwave dielectric properties. *J Alloys Compd* 2022, **898**: 162905.
[55] Šepelák V, Indris S, Bergmann I, *et al*. Nonequilibrium cation distribution in nanocrystalline $MgAl_2O_4$ spinel studied by ^{27}Al magic-angle spinning NMR. *Solid State Ionics* 2006, **177**: 2487–2490.
[56] Takahashi S, Kan A, Ogawa H. Microwave dielectric properties and crystal structures of spinel-structured $MgAl_2O_4$ ceramics synthesized by a molten-salt method. *J Eur Ceram Soc* 2017, **37**: 1001–1006.
[57] Fu P, Xu Y, Lu WZ, *et al*. Optical and microwave dielectric properties of Zn-doped $MgAl_2O_4$ transparent ceramics fabricated by spark plasma sintering. *Int J Appl Ceram Technol* 2015, **12**: 116–123.
[58] Wu SP, Xue JJ, Wang R, *et al*. Synthesis, characterization and microwave dielectric properties of spinel $MgGa_2O_4$ ceramic materials. *J Alloys Compd* 2014, **585**: 542–548.
[59] Yin J, Yang XZ, Lai YM, *et al*. Effects of $(Li_{0.5}Nb_{0.5})^{3+}$ co-substitution on microwave dielectric characteristics of $MgAl_2O_4$ ceramics. *J Cent South Univ* 2023, **30**: 1461–1468.
[60] Xue JJ, Wu SP, Li JH. Synthesis, microstructure, and microwave dielectric properties of spinel $ZnGa_2O_4$ ceramics. *J Am Ceram Soc* 2013, **96**: 2481–2485.
[61] Takahashi S, Kan A, Ogawa H. Effects of cation distribution on microwave dielectric properties of $Mg_{1-x}Zn_xAl_2O_4$ ceramics. *Mater Chem Phys* 2017, **200**: 257–263.
[62] Takahashi S, Kan A, Ogawa H. Microwave dielectric properties and crystal structures of $Mg_{0.7}Al_{2.2}O_4$ and $Mg_{0.4}Al_{2.4}O_4$ ceramics with defect structures. *J Am Ceram Soc* 2017, **100**: 3497–3504.
[63] He GQ, Ma XY, Liu YJ, *et al*. Sintering characteristics and microwave dielectric properties of ultralow-loss SrY_2O_4 ceramics. *Ceram Int* 2022, **48**: 21299–21304.
[64] Xie MJ, Li X, Lai YM, *et al*. Phase evolution and microware dielectric properties of high-entropy spinel-type $(Mg_{0.2}Co_{0.2}Ni_{0.2}Li_{0.4}Zn_{0.2})Al_2O_4$ ceramics. *J Eur Ceram Soc* 2024, **44**: 284–292.
[65] Shen SY, Tang Y, Li J, *et al*. Cation distribution and bond energy of intermediate spinel $Mg(Zn_{0.5}Ti_{0.5})_{2x}Ga_{(2-2x)}O_4$ microwave dielectric ceramics. *Ceram Int* 2021, **47**: 33731–33737.
[66] Roshni SB, Arun S, Sebastian MT, *et al*. Low κ Mg_2SiO_4 ceramic tapes and their role as screen printed microstrip patch antenna substrates. *Mater Sci Eng B—Adv* 2021, **264**: 114947.